

ORBITAL MOTION, VARIABILITY, AND MASSES IN THE T TAURI TRIPLE SYSTEM

G. H. SCHAEFER¹, TRACY L. BECK², L. PRATO³, & M. SIMON⁴

¹The CHARA Array of Georgia State University, Mount Wilson Observatory, Mount Wilson, CA 91023, USA; schaefer@chara-array.org

²Space Telescope Science Institute, 3700 San Martin Drive, Baltimore, MD 21218, USA

³Lowell Observatory, 1400 West Mars Hill Road, Flagstaff, AZ 86001, USA

⁴Department of Physics and Astronomy, Stony Brook University, Stony Brook, NY 11794, USA

ABSTRACT

We present results from adaptive optics imaging of the T Tauri triple system obtained at the Keck and Gemini Observatories in 2015–2019. We fit the orbital motion of T Tau Sb relative to Sa and model the astrometric motion of their center of mass relative to T Tau N. Using the distance measured by *Gaia*, we derived dynamical masses of $M_{\text{Sa}} = 2.05 \pm 0.14 M_{\odot}$ and $M_{\text{Sb}} = 0.43 \pm 0.06 M_{\odot}$. The precision in the masses is expected to improve with continued observations that map the motion through a complete orbital period; this is particularly important as the system approaches periastron passage in 2023. Based on published properties and recent evolutionary tracks, we estimate a mass of $\sim 2 M_{\odot}$ for T Tau N, suggesting that T Tau N is similar in mass to T Tau Sa. Narrow-band infrared photometry shows that T Tau N remained relatively constant between late 2017 and early 2019 with an average value of $K = 5.54 \pm 0.07$ mag. Using T Tau N to calibrate relative flux measurements since 2015, we found that T Tau Sa varied dramatically between 7.0 to 8.8 mag in the K -band over timescales of a few months, while T Tau Sb faded steadily from 8.5 to 11.1 mag in the K -band. Over the 27 year orbital period of the T Tau S binary, both components have shown 3–4 magnitudes of variability in the K -band, relative to T Tau N.

Keywords: binaries: visual — stars: fundamental parameters — stars: activity — stars: individual (T Tauri) — techniques: high angular resolution

1. INTRODUCTION

T Tauri is a young hierarchical triple system in the Taurus star forming region. The optically dominant component T Tau North (T Tau N) is the prototype for the class of T Tauri objects (Joy 1945) and has a spectral type of K0 (Luhman 2018). The infrared companion, T Tau South (T Tau S), was discovered at a separation of $\sim 0''.7$ (Dyck et al. 1982) and was subsequently revealed to be a close binary with a separation of $\sim 0''.05$ (Koresko 2000). The spectrum of T Tau Sa appears to be relatively featureless while T Tau Sb has the infrared spectrum of an early M star (Duchêne et al. 2002).

The orbital motion in the T Tau triple has been monitored for almost a complete period ($P \sim 27$ yr) over the past two decades (Köhler et al. 2000, 2008, 2016; Koresko 2000; Duchêne et al. 2002, 2005, 2006; Furlan et al. 2003; Beck et al. 2004; Mayama et al. 2006; Schaefer et al. 2006, 2014; Skemer et al. 2008; Ratzka et al. 2009; Csépany et al. 2015). Although T Tau N is one of the most massive and luminous T Tauri stars known and T Tau S is undetected in

the optical (Stapelfeldt et al. 1998), modeling the spectral energy distribution of T Tau S (Koresko et al. 1997) and mapping the orbital motion in the triple system (Duchêne et al. 2006; Köhler et al. 2008, 2016; Schaefer et al. 2014) suggest that T Tau Sa is at least as massive as T Tau N.

Along with the positions of the three components, high spatial resolution observations provide measurements of their relative fluxes. According to Beck et al. (2004), the near-infrared flux of T Tau N remained constant from 1994 to 2002. The first spatially resolved observations of T Tau Sa,Sb (Koresko 2000; Duchêne et al. 2006) occurred about a year after the last periastron passage ($T \sim 1996.1$). At the time of the discovery, T Tau Sa was about 2 mag brighter than Sb. During 2002–2007, the flux of T Tau Sa entered a highly variable phase where it ranged from ~ 2 mag fainter than Sb to 0.8 mag brighter than Sb. The variability of T Tau Sa then appeared to decrease through early 2014, while it remained fainter than Sb (Schaefer et al. 2014). Csépany et al. (2015) and Kasper et al. (2016) reported that T Tau Sa was again brighter than Sb in late 2014 through 2015.

Evidence suggests that T Tau Sa is enshrouded in a small (2–3 AU), moderately opaque, edge-on disk (Beck et al. 2004; Duchêne et al. 2005; Skemer et al. 2008; Manara et al. 2019). Beck et al. and Duchêne et al. speculated that changes in the brightness of Sa could be caused by variable extinction, where the star light intercepts thicker and thinner portions of the circumstellar disk as it rotates around the star. Alternatively, van Boekel et al. (2010) argue that the short-term variability is caused by variable accretion. They speculated that the enhanced variability in the early to late 1990’s was induced by a tidal perturbation of the disk following periastron passage. Plausibly, both phenomena could contribute to the system’s variability.

In this paper we present new adaptive optics (AO) measurements of the relative positions and fluxes of the components in the T Tau triple system obtained in 2015–2019. Based on these data and measurements in the literature, we compute an updated orbit fit to model the motion of T Tau Sb relative to Sa, as well as the motion of their center of mass relative to T Tau N. We derive dynamical masses of T Tau Sa and Sb from the orbital parameters. We also present photometry of the three components sampled at weekly to yearly timescales and discuss the variability of the system.

2. HIGH RESOLUTION NEAR-INFRARED IMAGING

2.1. Astrometry and Flux Ratios

AO imaging provides precise measurements of the orbital motion and relative flux ratios of the three components in the T Tau system. At the Keck Observatory, natural guide star AO observations were obtained using the NIRC2 narrow-field camera (Wizinowich et al. 2000) on the Keck II Telescope. At Gemini Observatory, observations were obtained using the Altair AO system and the NIRI f/32 camera (Hodapp et al. 2003). Images were recorded in the narrow-band *K* continuum filter during every epoch and in narrow-band *H* continuum and *L*-band emission line filters (Br α and PAH) during some epochs. The *K* and *H*-band images were flatfielded using dome flats. Sets of dithered images were recorded and subtracted to remove the background. In the *L*-band we created flats from the sky background in the science frames.

T Tau N was used as a simultaneous point spread function (PSF) reference to model the position and relative flux ratios of T Tau Sa and Sb (e.g., Schaefer et al. 2014). As shown in Figure 1, T Tau Sb was ~ 2 mag fainter than Sa during the observations, and the position of Sb lies near the diffraction ring of Sa. However, despite the challenge of resolving both components, Figure 2 demonstrates that we were able to recover the po-

sition of T Tau Sb using T Tau N as a simultaneous PSF to model the close pair.

For the Keck NIRC2 measurements, we corrected the binary positions using the geometric distortion solutions published by Yelda et al. (2010), prior to the optical realignment of the AO system on 2015 April 13, and by Service et al. (2016) after the realignment. For the pre-2015 observations, we used a plate scale of 9.952 ± 0.001 mas pixel $^{-1}$ and subtracted $0^\circ 252 \pm 0^\circ 009$ from the raw position angles to correct for the orientation of the camera relative to true north. After 2015 April 13, we used a plate scale of 9.971 ± 0.004 mas pixel $^{-1}$ and subtracted $0^\circ 262 \pm 0^\circ 020$ from the measured position angles. For the Gemini measurements we corrected for the radial barrel distortion¹ and applied a plate scale of 21.9 ± 0.1 mas and field orientation of $0^\circ 00 \pm 0^\circ 05$.

Table 1 reports the Julian year, binary separation (in milliarcseconds; mas), position angle measured east of north, and flux ratios measured in each filter for each pair of components in the T Tau system. The positions were averaged over the measurements from individual frames in the *K* continuum band, and uncertainties were computed from the standard deviation. During the observations, the separation of T Tau Sa,Sb was below the diffraction limit of the telescopes in the *L*-band, and the binary fit would not converge to a stable solution. Therefore, during the analysis of the *L*-band observations, we fixed the relative separation of T Tau Sa,Sb based on the *K*-band measurements during each epoch and solved for the flux ratios. In the *H*-band, the fluxes of T Tau Sa and Sb are very faint compared with T Tau N. Therefore we measured the flux ratio from a coadded image of all frames, but adopted uncertainties based on the standard deviation of fits to the individual frames.

We obtained two images of T Tau using the slit-viewing camera (SCAM) for the NIRSPEC spectrograph behind the AO system on the Keck II Telescope on UT 2020 Jan 30. We detected a component at a separation of ~ 673 mas and a flux ratio of ~ 0.18 relative to T Tau N, consistent with the last measured position of T Tau Sa in 2019.1. PSF fitting did not reveal the presence of T Tau Sb. However, in the first image, the center of T Tau N was partially saturated, and in the second, the signal-to-noise on the southern component was low, impacting our ability to detect Sb. By adding in a fake companion at the expected location of T Tau Sb and visually inspecting the images, we suspect that Sb is at least faint as it was in 2019.0 ($\gtrsim 3$ mag fainter than Sa).

2.2. Absolute Photometry

¹ <https://www.gemini.edu/instrumentation/niri/capability>

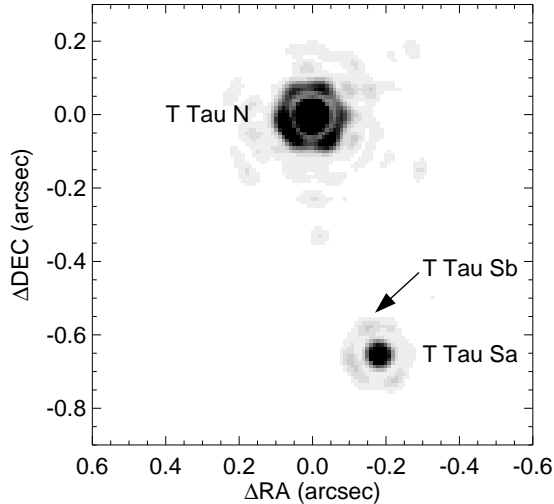


Figure 1. Coadded Keck AO image of the T Tau triple in the K continuum filter on UT 2019Jan20. The positions of T Tau N, Sa, and Sb are marked.

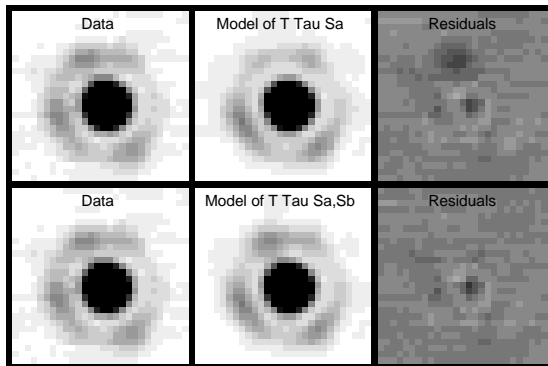


Figure 2. PSF fitting of T Tau Sa,Sb for a single Keck AO image obtained in the K cont filter on UT 2019Jan20. The top row shows the results of modeling only T Tau Sa as a single star using T Tau N as the PSF. The position of T Tau Sb jumps out in the residuals between the data and the model. The bottom panel shows the results of modeling both T Tau Sa and Sb as a binary using T Tau N as the PSF. The residuals show that T Tau Sb is fit cleanly.

On nights at the Gemini Observatory when conditions were photometric, observations were obtained of the near-infrared flux standard HD 22686. We performed aperture photometry using the `aper.pro` routine in the IDL astronomy library². We used an aperture radius of 100 pixels in the H con and K con filters, and a smaller radius typically of 60 pixels in the $Br\alpha$ filter to minimize the number of background counts at longer wavelengths. For T Tau, the aperture included the flux from all three components. We centered the aperture on T Tau N at H con and K con, because the northern component domi-

nates the light in these bands, and we centered half-way between T Tau N and S in $Br\alpha$ where the flux ratio of the northern and southern components are nearly equal.

We calibrated the total flux of T Tau by comparing with the flux measured on HD 22686. We did not apply a correction for airmass because the targets were observed at similar airmasses (Δz between targets ranged from 0.003 to 0.5) and the expected correction based on standard extinction curves (Tokunaga et al. 2002) is smaller than the uncertainties in the measured values. We used the narrow-band H con, K con, and $Br\alpha$ filters as proxies for the HKL fluxes. We computed the mean and standard deviation of the fluxes measured in the individual files and used sigma clipping to reject measurements that were more than 3σ discrepant from the mean. We calibrated the fluxes by adopting the magnitudes of $H = 7.186 \pm 0.009$ mag, $K = 7.186 \pm 0.008$ mag, and $L' = 7.199 \pm 0.008$ mag for the flux standard (Gutierrez et al. 2003; Leggett et al. 2003). We then used the relative fluxes reported in Table 1 to partition the total flux of T Tau into the magnitudes measured for each component. The absolute photometry is presented in Table 2.

The strength and variability of emission lines in the spectra of young stars complicates the comparison of magnitudes measured between the broadband and narrowband continuum filters. Using the narrowband filters was necessary to avoid saturation on T Tau in the Keck and Gemini AO images. Therefore, some caution is advised when comparing the magnitudes reported here to true broadband values. However, with the additional measurements presented in this paper, there is a growing set of relative flux measurements of the T Tau system in the narrow-band continuum filters (e.g., Schaefer et al. 2006) that can be used to study the variability of the components over the course of the orbital period of the close pair.

3. ORBITAL MOTION IN THE T TAU TRIPLE

We fit the relative orbit of T Tau Sa,Sb to the positions in Table 1 and measurements in the literature (Köhler et al. 2000, 2008, 2016; Koresko 2000; Duchêne et al. 2002, 2005, 2006; Furlan et al. 2003; Beck et al. 2004; Mayama et al. 2006; Schaefer et al. 2006, 2014; Skemer et al. 2008; Ratzka et al. 2009). We used a Newton-Raphson method to minimize χ^2 by calculating a first-order Taylor expansion for the equations of orbital motion. Table 3 lists the orbital parameters including the period P , time of periastron passage T , eccentricity e , angular semi-major axis a , inclination i , position angle of the line of nodes Ω , and argument of periastron ω . For visual binary orbits, there is a 180° ambiguity in the values of Ω and ω . This ambiguity can be resolved using radial velocity measurements to

² <https://idlastro.gsfc.nasa.gov/>

establish the direction of motion.

With all three components in the AO field of view, T Tau N serves as a reference to map the astrometric center-of-mass motion of the close pair. The astrometric motion provides the mass ratio of the close pair, $M_{\text{Sb}}/M_{\text{Sa}}$. We fit the astrometric motion by following the same approach outlined in Schaefer et al. (2012). We searched through a range of mass ratios to compute the expected location of the center of mass of T Tau Sa,Sb relative to N. For each trial mass ratio, we fit a representative orbit to the center of mass motion of S relative to N and selected the mass ratio that minimized the χ^2 between the calculated position of the center of mass and the orbit fit. An incorrect mass ratio will produce residual reflex motion that cannot be fit by a simple Keplerian orbit. We found a best fitting mass ratio of 0.210 ± 0.028 (Table 3). The relative and astrometric orbit fits are shown in Figure 3.

Figure 4 plots the residuals between the measured positions of T Tau Sb relative to Sa compared with the predictions from the orbit fit. There is significant scatter in the recent Gemini observations, especially as the separation of the close pair decreases below 90 mas in 2018.8 and later. As a check on the measured flux ratios, we fit a visual orbit for T Tau Sa,Sb to only the Keck observations and earlier measurements in the literature (excluding the Gemini observations reported here). We then computed the expected position of T Tau Sa,Sb at the time of the Gemini observations based on this orbit fit. Fixing the relative separation of the close Sa,Sb pair, we performed another PSF fit to the Gemini images and solved for the component flux ratios and separations relative to T Tau N. The flux ratios derived from the constrained fit are consistent within 1σ with the results reported in Table 1 (except for the Br α flux ratio in 2019.0410 which is discrepant by 1.6σ). This provides confidence that the flux ratios are likely reliable, despite the large scatter in the Gemini positions.

4. DYNAMICAL MASSES OF T TAU Sa AND Sb

The relative orbit of a binary system provides a measurement of the total mass if the distance is known. To derive masses of the components in T Tau, we used distances of 148.7 ± 1.0 pc measured from the trigonometric parallax with the Very Long Baseline Array (VLBA Galli et al. 2018) and 143.74 ± 1.22 pc derived from the *Gaia* Data Release 2 (DR2; Gaia Collaboration et al. 2018; Bailer-Jones et al. 2018). These two distance measurements are discrepant by 3σ , producing a systematic difference in the total mass derived for T Tau Sa and Sb, as shown in Table 4. Galli et al. (2019) discusses a comparison of several other sources that have both radio and *Gaia* parallaxes.

The VLBA parallax is based on mapping the motion

of the radio emission from T Tau Sb and must account for the orbital motion of Sb relative to Sa (Loinard et al. 2007; Galli et al. 2018). Galli et al. (2018) attempted to fit an acceleration term caused by the motion relative to T Tau N, but found this contribution to be negligible. Based on the orbit fit for the center-of-mass motion of T Tau S relative to T Tau N (see Sect. 5), we find a small acceleration term of $\sim 0.028 \text{ mas yr}^{-2}$ over the time frame of the VLBA observations. The *Gaia* parallax is based on the visible light from T Tau N; the measurement has a small amount of excess noise (0.12 mas). In the subsequent discussion we opt to use the masses derived from the *Gaia* distance because it is less complicated by the orbital motion of the close pair. The accuracy of the parallax should improve in the final *Gaia* data release.

Combining the mass ratio from the astrometric motion with the total mass from the relative orbit provides individual masses of $M_{\text{Sa}} = 2.05 \pm 0.14 M_{\odot}$ and $M_{\text{Sb}} = 0.43 \pm 0.06 M_{\odot}$. Currently the masses are measured with a precision of 6.7% and 12.7% for T Tau Sa and Sb, respectively. We expect the precision to improve to 2–5% by continuing to map the orbital motion for a complete orbital period through the next periastron passage (expected in 2023.3).

5. ORBIT OF T TAU S RELATIVE TO T TAU N

While fitting for the astrometric motion, we applied a constraint on the total system mass (N+Sa+Sb) when solving for the representative orbit of T Tau N,S. As discussed by Schaefer et al. (2006), a broad range of orbital parameters can be used to fit an orbit with limited coverage; often with a tail of eccentric solutions that yield very large masses. The constraint on the total mass of the system does not significantly impact the final value of the mass ratio of the close pair, however, it does provide a more realistic set of orbital parameters for the wide pair that can be used to predict and back-track the expected motion in the triple system.

We adopted the combined mass of T Tau Sa+Sb from the visual orbit and the *Gaia* distance ($M_{\text{Sa+Sb}} = 2.48 \pm 0.16 M_{\odot}$). We estimated the mass of T Tau N using the magnetic models of stellar evolution computed by Feiden (2016). We used the luminosity derived by Loinard et al. (2007) scaled to the *Gaia* distance (Bailer-Jones et al. 2018) and assumed an effective temperature of 5280 ± 60 K based on the spectral type of K0 adopted by Luhman (2018) and the temperature scale derived by Pecaute & Mamajek (2013). These stellar parameters correspond to a mass of $M_{\text{N}} = 2.03 \pm 0.12 M_{\odot}$ and an age of 3.8 ± 0.7 MY when compared with the evolutionary tracks, as shown in Figure 5.

High-resolution, infrared spectra of T Tau N in the *H*-band indicate a K5 spectral type for T Tau N (e.g.,

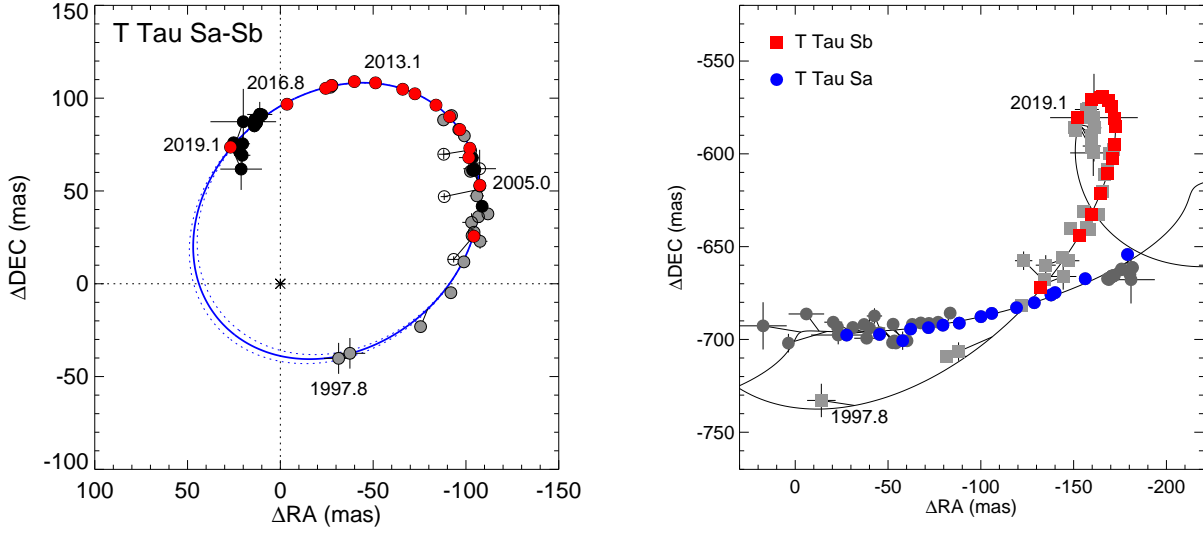


Figure 3. *Left:* Orbital motion of T Tau Sb relative to Sa. The red circles are Keck NIRC2 measurements presented in Table 1 and Schaefer et al. (2014). The black circles are Gemini NIRC2 measurements (this work; Beck et al. 2004; Schaefer et al. 2006). The gray circles are published values from the literature (Köhler et al. 2000, 2008, 2016; Koresko 2000; Duchêne et al. 2002, 2005, 2006; Furlan et al. 2003; Beck et al. 2004; Mayama et al. 2006; Skemer et al. 2008; Ratzka et al. 2009). The best fit orbit and uncertainties ($P = 27.18 \pm 0.72$ yr) are overplotted in solid and dotted blue lines, respectively. Four measurements with large residuals (Mayama et al. 2006; Skemer et al. 2008; Ratzka et al. 2009) were not included in the fit; these are plotted as open circles. Uncertainties are shown with crosses; for much of the data these are smaller than the points themselves. *Right:* Astrometric center-of-mass motion of T Tau Sa and Sb relative to T Tau N. The blue circles (T Tau Sa) and red squares (T Tau Sb) highlight the high precision astrometry from Keck. The dark gray circles (T Tau Sa) and light gray squares (T Tau Sb) show results from Gemini and the literature.

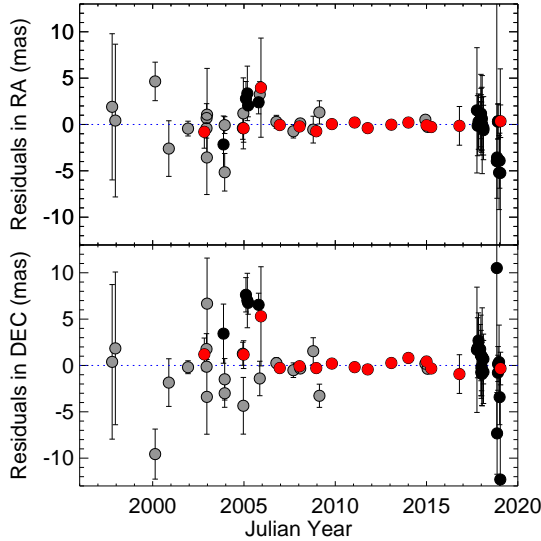


Figure 4. Residuals between the measured position of T Tau Sb relative to Sa and the orbit fit. The red circles are the Keck NIRC2 measurements, black circles are the Gemini NIRC2 measurements, and gray circles are from the literature.

R. Lopez-Valdivia et al. in prep; L. Prato in prep). The lower effective temperature, 4200–4400 K, implied by this result may represent the impact of starspots with a large filling factor on the photospheric flux (Gully-Santiago et al. 2017). Discussion of the discrep-

ancy between the K0 spectral type determined at optical wavelengths and the much later K5 type derived from infrared observations is beyond the scope of this paper and will be addressed in a forthcoming paper (L. Prato in prep).

When applying the constraint on the wide orbital motion, we limited the total system mass of the three components to be within $4.51 \pm 0.59 M_{\odot}$. The uncertainty corresponds to 3σ to provide a broader range of realistic values for the total mass. We also placed an arbitrary upper limit of $P < 5000$ yr on the orbital period. The best fit and range of orbital parameters that represent the motion of the center of mass of T Tau S relative to T Tau N are listed in Table 5 and plotted in Figure 6. These are consistent with the range of orbits for the wide pair found by Köhler et al. (2016).

If the effective temperature of T Tau N is lower than the value implied by the optical spectral type, then this would lead to a smaller mass for T Tau N. However, changing the total mass constraint based on where the effective temperature implied by the infrared spectral type of T Tau N intersects the evolutionary tracks in Figure 5 produces a similar range of possible orbital parameters for the wide N,S orbit. Moreover, the resulting masses of T Tau Sa and Sb change by only $0.003 M_{\odot}$, well within the 1σ uncertainty intervals reported in Table 4.

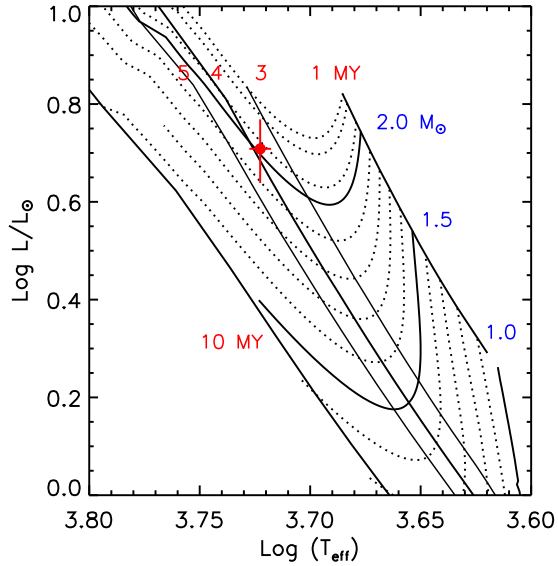


Figure 5. Evolutionary models computed by [Feiden \(2016\)](#) that include magnetic fields. The mass tracks are plotted at $0.1 M_{\odot}$ intervals from 1.0 to $2.0 M_{\odot}$ and then at 2.05 , 2.15 , and $2.20 M_{\odot}$. Three of the tracks are labeled in blue and shown as solid lines for 1.0 , 1.5 , and $2.0 M_{\odot}$. The isochrones are labeled in red and plotted at 1 , 3 , 4 , 5 , and 10 MY. The red circle shows the location of T Tau N (see Sect. 5).

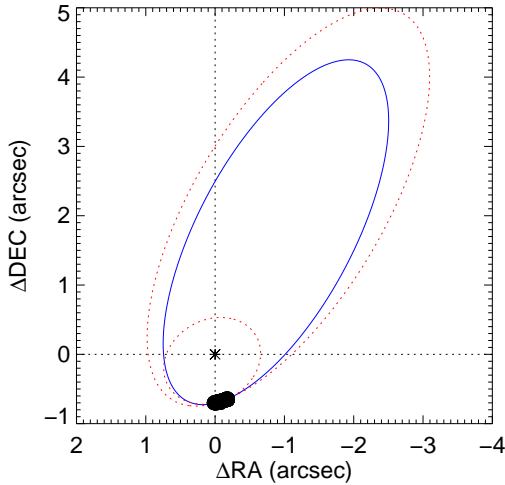


Figure 6. Orbital motion of T Tau S relative to N. The position of T Tau N is marked by the asterisk at the origin. The black circles show the measured positions computed for the center-of-mass of T Tau Sa,Sb. The blue line shows the best fit orbit while the red dotted lines show the range of orbital fits in Table 5.

6. VARIABILITY IN THE T TAU SYSTEM

The absolute photometric measurements from the Gemini observations (Table 2) are plotted in Figure 7. The K -band magnitude of T Tau N remained steady with a range of 5.45 – 5.65 mag and an average value of $K = 5.54 \pm 0.07$ mag. This is consistent with the results reported by [Beck et al. \(2004\)](#) who found that the

infrared flux of T Tau N remained constant from 1994 to 2002, with an average magnitude of $K = 5.53 \pm 0.03$ mag. The uncertainties at H and L are larger than at K because of the small flux of Sa and Sb in the H -band ($\gtrsim 6$ mag fainter than T Tau N), and the lower angular resolution in the L -band. T Tau N and Sa are similar in brightness in the L -band, but Sb is much fainter.

We can expand the time-frame of the variability measurements by assuming an average magnitude of $K = 5.53 \pm 0.03$ mag for T Tau N ([Beck et al. 2004](#)) and converting the relative flux ratios between the three components into magnitudes. The long-term brightness variations of T Tau Sa and Sb in the K -band are plotted in Figure 8. From 2015 to 2019, T Tau Sa experienced a dramatic increase in brightness, becoming ~ 2 mag brighter than Sb, continuing the brightening trend reported initially by [Csépany et al. \(2015\)](#) and [Kasper et al. \(2016\)](#). According to the Gemini observations that were taken with higher temporal sampling, the K -band magnitude of T Tau Sa dropped in early 2018 and then began rising again in late 2018 through early 2019. The K -band magnitude of T Tau Sb steadily decreased by ~ 2.6 mag over the 2015–2019 interval.

7. CONCLUSIONS

Based on our recent AO imaging of the T Tau triple system, combined with prior measurements in the literature, we fit the orbital motion of T Tau Sb relative to Sa and modeled the astrometric motion of their center of mass relative to T Tau N. Using the distance of 143.74 ± 1.22 pc ([Bailer-Jones et al. 2018](#)), we derived dynamical masses of $M_{\text{Sa}} = 2.05 \pm 0.14 M_{\odot}$ and $M_{\text{Sb}} = 0.43 \pm 0.06 M_{\odot}$. The orbital parameters, mass ratio, and masses are consistent within their uncertainties with the values computed by [Köhler et al. \(2016\)](#). However, the current uncertainties in the orbital parameters are significantly smaller thanks to the improved orbital coverage obtained over the past four years.

The fluxes derived from the AO images show that the K -band flux of T Tau N has remained steady between late 2017 and early 2019, with an average value of $K = 5.54 \pm 0.07$ mag. T Tau Sa is again brighter than Sb, but its K -band brightness varied dramatically in the past four years between 7.0 to 8.8 mag over timescales of a few months. On the other hand, T Tau Sb faded steadily from $K = 8.5$ to 11.1 mag over four years. In a forthcoming paper, T. Beck et al. (in prep) investigate the link between the variability, orbital motion, circumstellar emission, and outflows in the system.

We thank the staff at the Keck and Gemini observatories for their support during the observations. We also thank the referee for providing feedback that improved the paper. G.H.S. and L.P. acknowledge sup-

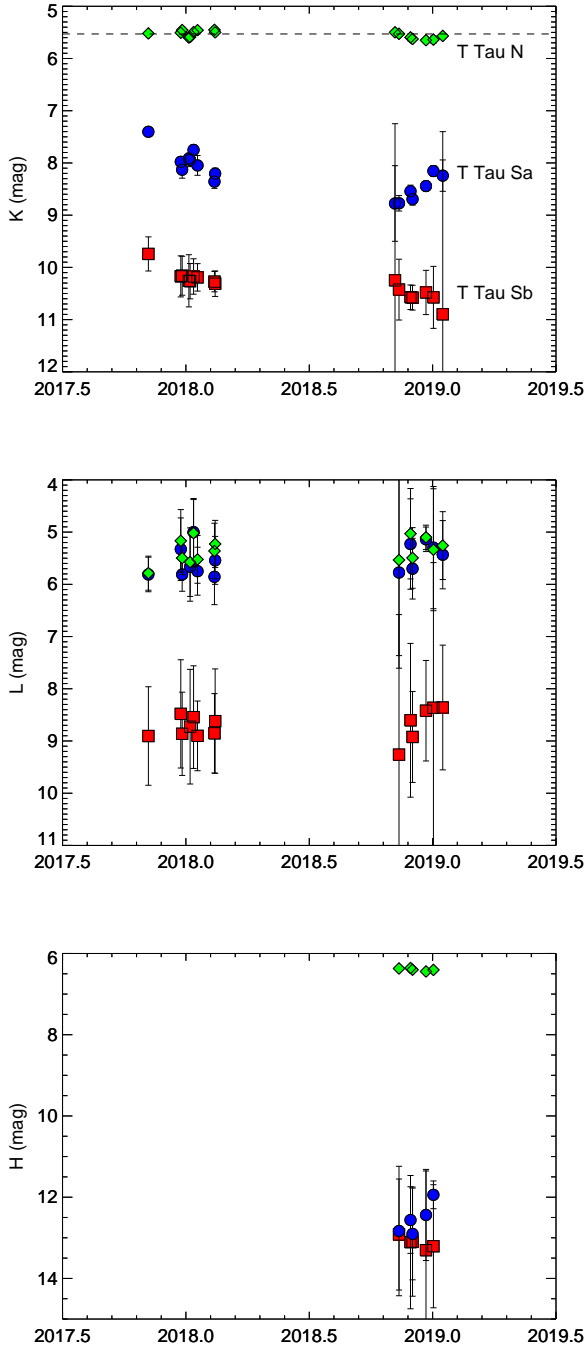


Figure 7. Magnitudes of T Tau N (green diamonds), Sa (blue circles), and Sb (red squares) based on Gemini AO observations on nights when the near-infrared flux standard HD 22686 was also observed (Sect. 2.2). The Kcon, Hcon, and Br α filters were used as a proxy for the KHL fluxes (top, middle, and bottom panels, respectively). The dashed line in the top panel corresponds to the mean magnitude of $K = 5.53 \pm 0.03$ determined by Beck et al. (2004).

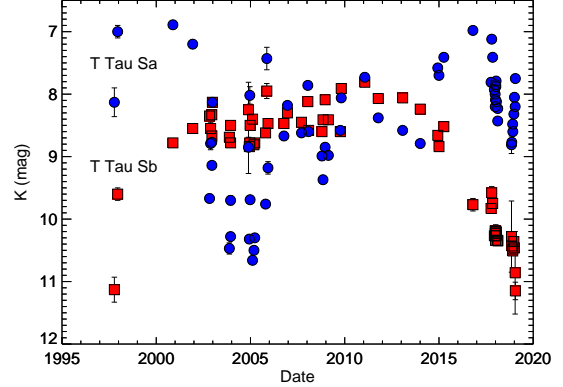


Figure 8. Variability of T Tau Sa (blue circles) and Sb (red squares) relative to T Tau N in the K -band. We derived the component magnitudes from the flux ratios and assumed a constant magnitude of $K = 5.53 \pm 0.03$ mag for T Tau N (Beck et al. 2004). The flux ratios are from Table 1 and measurements in the literature (Koresko 2000; Duchêne et al. 2002, 2005, 2006; Furlan et al. 2003; Beck et al. 2004; Mayama et al. 2006; Schaefer et al. 2006, 2014; van Boekel et al. 2010; Kasper et al. 2016).

port from NASA Keck PI Data Awards administered by the NASA Exoplanet Science Institute. Additional support was provided through the National Science Foundation (AST-1636624 for G.H.S. and AST-1518081 for L.P.). Some of the data presented herein were obtained at the W. M. Keck Observatory from telescope time allocated to the National Aeronautics and Space Administration through the agency’s scientific partnership with the California Institute of Technology and the University of California. The Observatory was made possible by the generous financial support of the W. M. Keck Foundation. Some of the observations were obtained at the Gemini Observatory (GN-2017B-Q-29, GN-2018B-Q-137), which is operated by the Association of Universities for Research in Astronomy, Inc., under a cooperative agreement with the NSF on behalf of the Gemini partnership: the National Science Foundation (United States), National Research Council (Canada), CONICYT (Chile), Ministerio de Ciencia, Tecnología e Innovación Productiva (Argentina), Ministério da Ciência, Tecnologia e Inovação (Brazil), and Korea Astronomy and Space Science Institute (Republic of Korea). Time at Gemini was granted through the time allocation process at the National Optical Astronomical Observatory (NOAO Prop. ID: 2017B-0280, 2018B-0321; PI: Schaefer). The data were downloaded through the Gemini Observatory Archive. We wish to recognize and acknowledge the significant cultural role that the summit of Maunakea has within the indigenous Hawaiian community. We are sincerely grateful for the opportunity to conduct these observations from the mountain. This research has made use of the SIMBAD database and the

VizieR catalog access tool, CDS, Strasbourg, France.

Facilities: Keck:II (NIRC2), Gemini:Gillett (NIRI)

REFERENCES

- Bailer-Jones, C. A. L., Rybizki, J., Fouesneau, M., Mantelet, G., & Andrae, R. 2018, *AJ*, 156, 58
- Beck, T. L., Schaefer, G. H., Simon, M., et al. 2004, *ApJ*, 614, 235
- Cs  p  ny, G., van den Ancker, M.,   brah  m, P., Brandner, W., & Hormuth, F. 2015, *A&A*, 578, L9
- Duch  ne, G., Beust, H., Adjali, F., Konopacky, Q. M., & Ghez, A. M. 2006, *A&A*, 457, L9
- Duch  ne, G., Ghez, A. M., & McCabe, C. 2002, *ApJ*, 568, 771
- Duch  ne, G., Ghez, A. M., McCabe, C., & Ceccarelli, C. 2005, *ApJ*, 628, 832
- Dyck, H. M., Simon, T., & Zuckerman, B. 1982, *ApJL*, 255, L103
- Feiden, G. A. 2016, *A&A*, 593, A99
- Furlan, E., Forrest, W. J., Watson, D. M., et al. 2003, *ApJL*, 596, L87
- Gaia Collaboration, Brown, A. G. A., Vallenari, A., et al. 2018, *A&A*, 616, A1
- Galli, P. A. B., Loinard, L., Ortiz-L  on, G. N., et al. 2018, *ApJ*, 859, 33
- Galli, P. A. B., Loinard, L., Bouy, H., et al. 2019, *A&A*, 630, A137
- Guetter, H. H., Vrba, F. J., Henden, A. A., & Luginbuhl, C. B. 2003, *AJ*, 125, 3344
- Gully-Santiago, M. A., Herczeg, G. J., Czekala, I., et al. 2017, *ApJ*, 836, 200
- Hodapp, K. W., Jensen, J. B., Irwin, E. M., et al. 2003, *PASP*, 115, 1388
- Joy, A. H. 1945, *ApJ*, 102, 168
- Kasper, M., Santhakumari, K. K. R., Herbst, T. M., & K  hler, R. 2016, *A&A*, 593, A50
- K  hler, R., Kasper, M., & Herbst, T. 2000, in *Birth and Evolution of Binary Stars: Poster Proceedings of IAU Symposium No. 200 on the Formation of Binary Stars*, ed. B. Reipurth & H. Zinnecker (Potsdam, Germany: Astrophysikalisches Institut Potsdam), 63
- K  hler, R., Kasper, M., Herbst, T. M., Ratzka, T., & Bertrang, G. H. M. 2016, *A&A*, 587, A35
- K  hler, R., Ratzka, T., Herbst, T. M., & Kasper, M. 2008, *A&A*, 482, 929
- Koresko, C. D. 2000, *ApJL*, 531, L147
- Koresko, C. D., Herbst, T. M., & Leinert, C. 1997, *ApJ*, 480, 741
- Leggett, S. K., Hawarden, T. G., Currie, M. J., et al. 2003, *MNRAS*, 345, 144
- Loinard, L., Torres, R. M., Mioduszewski, A. J., et al. 2007, *ApJ*, 671, 546
- Luhman, K. L. 2018, *AJ*, 156, 271
- Manara, C. F., Tazzari, M., Long, F., et al. 2019, *A&A*, 628, A95
- Mayama, S., Tamura, M., Hayashi, M., et al. 2006, *PASJ*, 58, 375
- Pecaut, M. J., & Mamajek, E. E. 2013, *ApJS*, 208, 9
- Ratzka, T., Schegerer, A. A., Leinert, C., et al. 2009, *A&A*, 502, 623
- Schaefer, G. H., Prato, L., Simon, M., & Patience, J. 2014, *AJ*, 147, 157
- Schaefer, G. H., Prato, L., Simon, M., & Zavala, R. T. 2012, *ApJ*, 756, 120
- Schaefer, G. H., Simon, M., Beck, T. L., Nelan, E., & Prato, L. 2006, *AJ*, 132, 2618
- Service, M., Lu, J. R., Campbell, R., et al. 2016, *PASP*, 128, 095004
- Skemer, A. J., Close, L. M., Hinz, P. M., et al. 2008, *ApJ*, 676, 1082
- Stapelfeldt, K. R., Burrows, C. J., Krist, J. E., et al. 1998, *ApJ*, 508, 736
- Tokunaga, A. T., Simons, D. A., & Vacca, W. D. 2002, *PASP*, 114, 180
- van Boekel, R., Juh  sz, A., Henning, T., et al. 2010, *A&A*, 517, A16
- Wizinowich, P., Acton, D. S., Shelton, C., et al. 2000, *PASP*, 112, 315
- Yelda, S., Lu, J. R., Ghez, A. M., et al. 2010, *ApJ*, 725, 331

Table 1. Near-IR Adaptive Optics Measurements of T Tau Triple System

UT Date	JY	Pair	$\rho(\text{mas})$	P.A.($^{\circ}$)	Filter	Flux Ratio	Tel ^a
2015Jan01	2015.0000	Sa,Sb	110.34 \pm 0.55	345.52 \pm 0.29	Kcont	0.3491 \pm 0.0078	K
					Hcont	2.9314 \pm 0.5648	K
2015Apr05	2015.2573	Sa,Sb	108.09 \pm 0.40	346.94 \pm 0.21	Kcont	0.3612 \pm 0.0067	K
2016Oct20	2016.8021	Sa,Sb	96.79 \pm 2.09	357.88 \pm 1.24	Kcont	0.0768 \pm 0.0066	K
					Hcont	0.1572 \pm 0.0372	K
2017Oct05	2017.7605	Sa,Sb	91.89 \pm 6.76	6.94 \pm 4.21	Kcon	0.1554 \pm 0.0127	G
					BrA	0.0823 \pm 0.0189	G
2017Oct19	2017.7989	Sa,Sb	91.60 \pm 3.24	6.25 \pm 2.03	Kcon	0.1033 \pm 0.0099	G
					BrA	0.0527 \pm 0.0081	G
2017Nov06	2017.8479	Sa,Sb	92.00 \pm 2.99	6.91 \pm 1.86	Kcon	0.1160 \pm 0.0073	G
					BrA	0.0579 \pm 0.0091	G
2017Dec09	2017.9382	Sa,Sb	90.24 \pm 2.67	7.50 \pm 1.69	Kcon	0.1152 \pm 0.0083	G
					BrA	0.0492 \pm 0.0083	G
2017Dec24	2017.9792	Sa,Sb	89.40 \pm 4.35	8.74 \pm 2.79	Kcon	0.1326 \pm 0.0094	G
					BrA	0.0548 \pm 0.0082	G
2017Dec26	2017.9848	Sa,Sb	89.36 \pm 2.72	8.87 \pm 1.74	Kcon	0.1543 \pm 0.0115	G
					BrA	0.0602 \pm 0.0079	G
2017Dec31	2017.9983	Sa,Sb	87.34 \pm 2.81	8.68 \pm 1.84	Kcon	0.1260 \pm 0.0097	G
2018Jan05	2018.0120	Sa,Sb	87.74 \pm 2.59	8.38 \pm 1.69	Kcon	0.1158 \pm 0.0115	G
2018Jan07	2018.0170	Sa,Sb	87.54 \pm 2.97	8.54 \pm 1.94	Kcon	0.1178 \pm 0.0081	G
					BrA	0.0597 \pm 0.0093	G
2018Jan12	2018.0310	Sa,Sb	86.91 \pm 3.38	9.17 \pm 2.23	Kcon	0.1073 \pm 0.0072	G
					BrA	0.0382 \pm 0.0050	G
2018Jan18	2018.0471	Sa,Sb	88.50 \pm 5.29	8.72 \pm 3.42	Kcon	0.1391 \pm 0.0093	G
					BrA	0.0548 \pm 0.0050	G
2018Feb12	2018.1158	Sa,Sb	87.58 \pm 2.69	9.03 \pm 1.76	Kcon	0.1714 \pm 0.0070	G
					BrA	0.0633 \pm 0.0065	G
2018Feb13	2018.1186	Sa,Sb	86.21 \pm 3.40	9.34 \pm 2.26	Kcon	0.1434 \pm 0.0069	G
					BrA	0.0588 \pm 0.0100	G
2018Nov06	2018.8475	Sa,Sb	89.56 \pm 17.69	12.88 \pm 11.32	Kcon	0.2848 \pm 0.2446	G
					BrA	0.0277 \pm 0.0120	G
2018Nov12	2018.8637	Sa,Sb	72.23 \pm 4.41	16.55 \pm 3.50	Kcon	0.2189 \pm 0.0266	G
					BrA	0.0404 \pm 0.0141	G
					Hcon	0.9231 \pm 0.5198	G
2018Nov29	2018.9103	Sa,Sb	79.20 \pm 1.89	18.42 \pm 1.37	Kcon	0.1543 \pm 0.0071	G
					BrA	0.0447 \pm 0.0094	G
					Hcon	0.6061 \pm 0.2147	G
2018Dec02	2018.9186	Sa,Sb	80.03 \pm 1.89	18.34 \pm 1.35	Kcon	0.1762 \pm 0.0097	G
					BrA	0.0514 \pm 0.0060	G
					Hcon	0.8400 \pm 0.2729	G
2018Dec22	2018.9731	Sa,Sb	78.11 \pm 3.99	15.08 \pm 2.93	Kcon	0.1531 \pm 0.0120	G
					BrA	0.0487 \pm 0.0080	G
					Hcon	0.4500 \pm 0.2636	G
2019Jan02	2019.0032	Sa,Sb	74.52 \pm 2.97	17.16 \pm 2.28	Kcon	0.1078 \pm 0.0116	G
					BrA	0.0596 \pm 0.0276	G
					Hcon	0.3115 \pm 0.0747	G
2019Jan16	2019.0410	Sa,Sb	65.29 \pm 11.23	18.88 \pm 9.86	Kcon	0.0900 \pm 0.0705	G
					BrA	0.0677 \pm 0.0125	G
2019Jan20	2019.0520	Sa,Sb	78.34 \pm 1.76	20.04 \pm 1.29	Kcont	0.0438 \pm 0.0057	K

Table 1 continued

Table 1 (*continued*)

UT Date	JY	Pair	$\rho(\text{mas})$	P.A.($^{\circ}$)	Filter	Flux Ratio	Tel ^a
					Hcont	0.0816 \pm 0.0693	K
					PAH	0.0210 \pm 0.0057	K
2015Jan01	2015.0000	N,Sa	689.91 \pm 0.72	191.524 \pm 0.061	Kcont	0.1353 \pm 0.0021	K
					Hcont	0.0038 \pm 0.0006	K
2015Apr05	2015.2573	N,Sa	689.17 \pm 0.43	191.721 \pm 0.037	Kcont	0.1768 \pm 0.0011	K
2016Oct20	2016.8021	N,Sa	685.34 \pm 0.53	193.179 \pm 0.048	Kcont	0.2631 \pm 0.0035	K
					Hcont	0.0159 \pm 0.0006	K
2017Oct05	2017.7605	N,Sa	688.19 \pm 0.98	194.151 \pm 0.096	Kcon	0.1226 \pm 0.0026	G
					BrA	1.1090 \pm 0.0186	G
2017Oct19	2017.7989	N,Sa	688.79 \pm 1.16	194.201 \pm 0.108	Kcon	0.2315 \pm 0.0030	G
					BrA	1.1723 \pm 0.0083	G
2017Nov06	2017.8479	N,Sa	688.00 \pm 0.86	194.221 \pm 0.087	Kcon	0.1765 \pm 0.0023	G
					BrA	0.9774 \pm 0.0103	G
2017Dec09	2017.9382	N,Sa	687.81 \pm 0.81	194.325 \pm 0.084	Kcon	0.1099 \pm 0.0020	G
					BrA	0.8732 \pm 0.0080	G
2017Dec24	2017.9792	N,Sa	687.74 \pm 0.80	194.348 \pm 0.083	Kcon	0.1027 \pm 0.0016	G
					BrA	0.8629 \pm 0.0053	G
2017Dec26	2017.9848	N,Sa	687.31 \pm 1.25	194.376 \pm 0.115	Kcon	0.0852 \pm 0.0022	G
					BrA	0.7487 \pm 0.0073	G
2017Dec31	2017.9983	N,Sa	687.39 \pm 1.18	194.374 \pm 0.110	Kcon	0.0950 \pm 0.0015	G
2018Jan05	2018.0120	N,Sa	687.40 \pm 0.97	194.375 \pm 0.095	Kcon	0.1185 \pm 0.0020	G
2018Jan07	2018.0170	N,Sa	687.35 \pm 0.92	194.369 \pm 0.091	Kcon	0.1145 \pm 0.0026	G
					BrA	0.9198 \pm 0.0062	G
2018Jan12	2018.0310	N,Sa	687.55 \pm 0.82	194.410 \pm 0.085	Kcon	0.1253 \pm 0.0020	G
					BrA	1.0181 \pm 0.0058	G
2018Jan18	2018.0471	N,Sa	687.63 \pm 0.92	194.391 \pm 0.091	Kcon	0.0921 \pm 0.0030	G
					BrA	0.8120 \pm 0.0080	G
2018Feb12	2018.1158	N,Sa	687.40 \pm 0.84	194.483 \pm 0.086	Kcon	0.0689 \pm 0.0014	G
					BrA	0.6342 \pm 0.0058	G
2018Feb13	2018.1186	N,Sa	687.44 \pm 0.95	194.471 \pm 0.093	Kcon	0.0828 \pm 0.0014	G
					BrA	0.7490 \pm 0.0114	G
2018Nov06	2018.8475	N,Sa	691.88 \pm 12.82	195.159 \pm 1.063	Kcon	0.0489 \pm 0.0062	G
					BrA	0.7954 \pm 0.0087	G
2018Nov12	2018.8637	N,Sa	689.04 \pm 1.40	195.171 \pm 0.127	Kcon	0.0504 \pm 0.0012	G
					BrA	0.8019 \pm 0.0105	G
					Hcon	0.0026 \pm 0.0007	G
2018Nov29	2018.9103	N,Sa	685.37 \pm 0.88	194.866 \pm 0.089	Kcon	0.0663 \pm 0.0011	G
					BrA	0.8334 \pm 0.0050	G
					Hcon	0.0033 \pm 0.0005	G
2018Dec02	2018.9186	N,Sa	684.98 \pm 0.99	194.871 \pm 0.097	Kcon	0.0593 \pm 0.0011	G
					BrA	0.8275 \pm 0.0055	G
					Hcon	0.0025 \pm 0.0005	G
2018Dec22	2018.9731	N,Sa	685.82 \pm 1.14	195.335 \pm 0.107	Kcon	0.0764 \pm 0.0012	G
					BrA	0.9663 \pm 0.0047	G
					Hcon	0.0040 \pm 0.0008	G
2019Jan02	2019.0032	N,Sa	685.70 \pm 0.92	195.351 \pm 0.091	Kcon	0.0985 \pm 0.0014	G
					BrA	1.0380 \pm 0.0155	G
					Hcon	0.0061 \pm 0.0004	G
2019Jan16	2019.0410	N,Sa	685.79 \pm 1.81	195.364 \pm 0.159	Kcon	0.0852 \pm 0.0045	G
					BrA	0.8511 \pm 0.0114	G
2019Jan20	2019.0520	N,Sa	678.29 \pm 0.44	195.305 \pm 0.042	Kcont	0.1294 \pm 0.0014	K

Table 1 *continued*

Table 1 (*continued*)

UT Date	JY	Pair	$\rho(\text{mas})$	P.A.($^\circ$)	Filter	Flux Ratio	Tel ^a
					Hcont	0.0049 \pm 0.0003	K
					PAH	0.4007 \pm 0.0065	K
2015Jan01	2015.0000	N,Sb	592.72 \pm 0.78	196.205 \pm 0.076	Kcont	0.0472 \pm 0.0009	K
					Hcont	0.0109 \pm 0.0009	K
2015Apr05	2015.2573	N,Sb	592.76 \pm 0.61	196.105 \pm 0.060	Kcont	0.0639 \pm 0.0008	K
2016Oct20	2016.8021	N,Sb	592.53 \pm 2.31	195.650 \pm 0.224	Kcont	0.0202 \pm 0.0018	K
					Hcont	0.0025 \pm 0.0006	K
2017Oct05	2017.7605	N,Sb	597.14 \pm 6.44	195.257 \pm 0.619	Kcon	0.0190 \pm 0.0013	G
					BrA	0.0912 \pm 0.0204	G
2017Oct19	2017.7989	N,Sb	598.21 \pm 3.47	195.415 \pm 0.336	Kcon	0.0239 \pm 0.0020	G
					BrA	0.0617 \pm 0.0092	G
2017Nov06	2017.8479	N,Sb	596.86 \pm 2.69	195.345 \pm 0.263	Kcon	0.0205 \pm 0.0012	G
					BrA	0.0566 \pm 0.0088	G
2017Dec09	2017.9382	N,Sb	598.30 \pm 2.80	195.351 \pm 0.273	Kcon	0.0126 \pm 0.0009	G
					BrA	0.0429 \pm 0.0070	G
2017Dec24	2017.9792	N,Sb	598.83 \pm 4.24	195.184 \pm 0.409	Kcon	0.0136 \pm 0.0009	G
					BrA	0.0473 \pm 0.0070	G
2017Dec26	2017.9848	N,Sb	598.43 \pm 3.46	195.196 \pm 0.335	Kcon	0.0131 \pm 0.0008	G
					BrA	0.0451 \pm 0.0057	G
2017Dec31	2017.9983	N,Sb	600.55 \pm 3.31	195.200 \pm 0.320	Kcon	0.0120 \pm 0.0008	G
2018Jan05	2018.0120	N,Sb	600.21 \pm 3.23	195.250 \pm 0.312	Kcon	0.0137 \pm 0.0012	G
2018Jan07	2018.0170	N,Sb	600.32 \pm 2.96	195.218 \pm 0.286	Kcon	0.0135 \pm 0.0008	G
					BrA	0.0549 \pm 0.0084	G
2018Jan12	2018.0310	N,Sb	601.06 \pm 3.36	195.166 \pm 0.324	Kcon	0.0134 \pm 0.0008	G
					BrA	0.0389 \pm 0.0050	G
2018Jan18	2018.0471	N,Sb	599.63 \pm 5.05	195.226 \pm 0.485	Kcon	0.0128 \pm 0.0006	G
					BrA	0.0445 \pm 0.0038	G
2018Feb12	2018.1158	N,Sb	600.27 \pm 2.83	195.278 \pm 0.275	Kcon	0.0118 \pm 0.0004	G
					BrA	0.0401 \pm 0.0038	G
2018Feb13	2018.1186	N,Sb	601.62 \pm 3.46	195.206 \pm 0.333	Kcon	0.0119 \pm 0.0005	G
					BrA	0.0440 \pm 0.0068	G
2018Nov06	2018.8475	N,Sb	602.40 \pm 23.61	195.497 \pm 2.246	Kcon	0.0126 \pm 0.0066	G
					BrA	0.0220 \pm 0.0095	G
2018Nov12	2018.8637	N,Sb	616.83 \pm 4.84	195.010 \pm 0.452	Kcon	0.0110 \pm 0.0011	G
					BrA	0.0323 \pm 0.0110	G
					Hcon	0.0024 \pm 0.0006	G
2018Nov29	2018.9103	N,Sb	606.35 \pm 2.17	194.402 \pm 0.211	Kcon	0.0102 \pm 0.0004	G
					BrA	0.0372 \pm 0.0077	G
					Hcon	0.0020 \pm 0.0006	G
2018Dec02	2018.9186	N,Sb	605.12 \pm 2.38	194.413 \pm 0.231	Kcon	0.0104 \pm 0.0004	G
					BrA	0.0425 \pm 0.0048	G
					Hcon	0.0021 \pm 0.0005	G
2018Dec22	2018.9731	N,Sb	607.71 \pm 3.84	195.368 \pm 0.365	Kcon	0.0117 \pm 0.0009	G
					BrA	0.0470 \pm 0.0077	G
					Hcon	0.0018 \pm 0.0006	G
2019Jan02	2019.0032	N,Sb	611.22 \pm 2.98	195.131 \pm 0.284	Kcon	0.0106 \pm 0.0011	G
					BrA	0.0615 \pm 0.0271	G
					Hcon	0.0019 \pm 0.0005	G
2019Jan16	2019.0410	N,Sb	620.63 \pm 12.43	194.994 \pm 1.149	Kcon	0.0074 \pm 0.0045	G
					BrA	0.0575 \pm 0.0101	G
2019Jan20	2019.0520	N,Sb	600.26 \pm 1.75	194.688 \pm 0.168	Kcont	0.0057 \pm 0.0007	K

Table 1 *continued*

Table 1 (*continued*)

UT Date	JY	Pair	$\rho(\text{mas})$	P.A.($^\circ$)	Filter	Flux Ratio	Tel ^a
					Hcont	0.0004 \pm 0.0003	K
					PAH	0.0084 \pm 0.0022	K

^aThe last column identifies the telescope used: G = Gemini North, K = Keck II.

Table 2. Absolute photometry based on Gemini observations of T Tau.

JY	Filter	N	Sa	Sb
2017.8479	<i>K</i>	5.52 \pm 0.04	7.40 \pm 0.08	9.74 \pm 0.33
2017.9792	<i>K</i>	5.51 \pm 0.03	7.98 \pm 0.09	10.17 \pm 0.39
2017.9848	<i>K</i>	5.46 \pm 0.06	8.13 \pm 0.16	10.16 \pm 0.37
2018.0120	<i>K</i>	5.60 \pm 0.03	7.91 \pm 0.10	10.26 \pm 0.50
2018.0170	<i>K</i>	5.59 \pm 0.03	7.94 \pm 0.13	10.26 \pm 0.34
2018.0310	<i>K</i>	5.50 \pm 0.03	7.75 \pm 0.10	10.17 \pm 0.34
2018.0471	<i>K</i>	5.46 \pm 0.04	8.05 \pm 0.19	10.19 \pm 0.26
2018.1158	<i>K</i>	5.45 \pm 0.06	8.36 \pm 0.13	10.27 \pm 0.20
2018.1186	<i>K</i>	5.50 \pm 0.03	8.20 \pm 0.10	10.31 \pm 0.24
2018.8475	<i>K</i>	5.50 \pm 0.04	8.78 \pm 0.72	10.25 \pm 3.00
2018.8637	<i>K</i>	5.53 \pm 0.05	8.77 \pm 0.15	10.43 \pm 0.58
2018.9103	<i>K</i>	5.60 \pm 0.07	8.54 \pm 0.12	10.57 \pm 0.23
2018.9186	<i>K</i>	5.63 \pm 0.03	8.69 \pm 0.11	10.58 \pm 0.24
2018.9731	<i>K</i>	5.65 \pm 0.03	8.44 \pm 0.09	10.48 \pm 0.42
2019.0032	<i>K</i>	5.64 \pm 0.07	8.16 \pm 0.10	10.57 \pm 0.59
2019.0410	<i>K</i>	5.57 \pm 0.03	8.24 \pm 0.30	10.90 \pm 3.50
2017.8479	<i>L</i>	5.79 \pm 0.33	5.81 \pm 0.33	8.90 \pm 0.94
2017.9792	<i>L</i>	5.17 \pm 0.60	5.33 \pm 0.60	8.48 \pm 1.04
2017.9848	<i>L</i>	5.50 \pm 0.32	5.81 \pm 0.32	8.86 \pm 0.80
2018.0170	<i>L</i>	5.58 \pm 0.66	5.67 \pm 0.66	8.73 \pm 1.10
2018.0310	<i>L</i>	5.02 \pm 0.64	5.00 \pm 0.64	8.54 \pm 0.98
2018.0471	<i>L</i>	5.52 \pm 0.46	5.75 \pm 0.46	8.90 \pm 0.67
2018.1158	<i>L</i>	5.36 \pm 0.53	5.86 \pm 0.53	8.85 \pm 0.76
2018.1186	<i>L</i>	5.23 \pm 0.45	5.54 \pm 0.46	8.62 \pm 1.00
2018.8637	<i>L</i>	5.53 \pm 1.83	5.77 \pm 1.83	9.26 \pm 2.68
2018.9103	<i>L</i>	5.03 \pm 0.87	5.23 \pm 0.87	8.60 \pm 1.47
2018.9186	<i>L</i>	5.49 \pm 0.58	5.70 \pm 0.58	8.92 \pm 0.87
2018.9731	<i>L</i>	5.10 \pm 0.23	5.14 \pm 0.24	8.42 \pm 0.96
2019.0032	<i>L</i>	5.34 \pm 1.17	5.30 \pm 1.17	8.36 \pm 2.78
2019.0410	<i>L</i>	5.26 \pm 0.65	5.43 \pm 0.65	8.36 \pm 1.19
2018.8637	<i>H</i>	6.37 \pm 0.03	12.83 \pm 1.59	12.92 \pm 1.37
2018.9103	<i>H</i>	6.36 \pm 0.04	12.56 \pm 0.82	13.11 \pm 1.64
2018.9186	<i>H</i>	6.40 \pm 0.06	12.91 \pm 1.13	13.09 \pm 1.34
2018.9731	<i>H</i>	6.44 \pm 0.04	12.44 \pm 1.12	13.30 \pm 1.95
2019.0032	<i>H</i>	6.41 \pm 0.04	11.94 \pm 0.34	13.21 \pm 1.51

Table 3. Orbital parameters of T Tau Sa,Sb

Parameter	Value
P (yr)	27.18 ± 0.72
T (JY)	1996.10 ± 0.38
e	0.551 ± 0.032
a (mas)	85.12 ± 0.62
i ($^\circ$)	21.1 ± 2.1
Ω ($^\circ$)	94.4 ± 16.9
ω ($^\circ$)	45.8 ± 16.9
$M_{\text{Sb}}/M_{\text{Sa}}$	0.210 ± 0.028

Table 4. Dynamical Masses of T Tau Sa and Sb

Parameter	VLBA Parallax	Gaia Parallax
Adopted d (pc)	148.7 ± 1.0	143.74 ± 1.22
Reference	Galli et al. (2018)	Bailer-Jones et al. (2018)
$M_{\text{Sa+Sb}}(M_\odot)$	2.744 ± 0.166	2.479 ± 0.155
$M_{\text{Sa}}(M_\odot)$	2.268 ± 0.147	2.049 ± 0.137
$M_{\text{Sb}}(M_\odot)$	0.476 ± 0.060	0.430 ± 0.055

Table 5. Range of Orbital Parameters for T Tau N,S

Parameter	Best Fit	Range
P (yr)	4602.6	481 – 4997
T (JY)	1951.3	1697 – 2344
e	0.754	0.00 – 0.79
a (mas)	3255.1	733 – 3426
i ($^\circ$)	54.2	29 – 60
Ω ($^\circ$)	148.2	70 – 164
ω ($^\circ$)	10.4	0 – 360

NOTE—We applied a constraint of $4.51 \pm 0.59 M_\odot$ on the total mass of N+Sa+Sb and an upper limit on the period of 5000 yr.